Monthly Notices of the ROYAL ASTRONOMICAL SOCIETY

MNRAS **451,** 3920–3932 (2015) doi:10.1093/mnras/stv1168

Hubble Frontier Field free-form mass mapping of the massive multiple-merging cluster MACSJ0717.5+3745

Jose M. Diego,[1]★ Tom Broadhurst,[2,3] Adi Zitrin,[4]† Daniel Lam,[5] Jeremy Lim,[5] Holland C. Ford[6] and Wei Zheng[6]

[1]*IFCA, Instituto de Física de Cantabria (UC-CSIC), Av. de Los Castros s/n, E-39005 Santander, Spain*
[2]*Fisika Teorikoa, Zientzia eta Teknologia Fakultatea, Euskal Herriko Unibertsitatea UPV/EHU, E-48080 Bilbao, Spain*
[3]*IKERBASQUE, Basque Foundation for Science, Alameda Urquijo 36-5, E-48008 Bilbao, Spain*
[4]*Cahill Center for Astronomy and Astrophysics, California Institute of Technology, MS 249-17, Pasadena, CA 91125, USA*
[5]*Department of Physics, The University of Hong Kong, 0000-0002-6536-5575, Pokfulam Road, Hong Kong*
[6]*Department of Physics and Astronomy, Johns Hopkins University, Baltimore, MD 21218, USA*

Accepted 2015 May 20. Received 2015 April 23; in original form 2014 November 11

ABSTRACT

We examine the latest data on the cluster MACSJ0717.5+3745 from the Hubble Frontier Fields campaign. The critically lensed area is the largest known of any lens and very irregular making it a challenge for parametric modelling. Using our free-form method we obtain an accurate solution, identify here many new sets of multiple images, doubling the number of constraints and improving the reconstruction of the dark matter distribution. Our reconstructed mass map shows several distinct central substructures with shallow density profiles, clarifying earlier work and defining well the relation between the dark matter distribution and the luminous and X-ray peaks within the critically lensed region. Using our free-form method, we are able to meaningfully subtract the mass contribution from cluster members to the deflection field to trace the smoothly distributed cluster dark matter distribution. We find four distinct concentrations, three of which are coincident with the luminous matter. The fourth peak has a significant offset from both the closest luminous and X-ray peaks. These findings, together with dynamical data from the motions of galaxies and gas will be important for uncovering the potentially important implications of this extremely massive and intriguing system.

Key words: galaxies: clusters: general – dark matter.

1 INTRODUCTION

The standard model of structure formation is built on the conclusion that about 85 per cent of the mass in the Universe is of an unknown form which only gravitates. The standard interpretation of this dark matter (DM) as massive fermionic particles has, so far, no experimental evidence from sensitive direct searches via nuclear recoil (Akerib et al. 2014) nor have such particles been generated at high energies with the LHC. Astronomically, the most extreme effects of dark matter can be found in massive galaxy clusters, where the general relativistic warping of space–time leads to extreme lensing distortions on a scale far in excess of that due to the observed stellar or gaseous cluster material. Among all known clusters, MACSJ0717.5+3745 (MACS0717 hereafter, Ebeling et al. 2007) is one of the most massive and extreme clusters in terms of its mass and temperature, with light deflections of over an arcminute discovered by (Zitrin et al. 2009, hereafter Z09). This cluster has been extensively studied from a multiwavelength perspective providing a unique opportunity to explore the interplay between the visible and DM.

Radio observations reveal that this cluster hosts one the most powerful radio haloes known to date (Bonafede et al. 2009; van Weeren et al. 2009; Pandey-Pommier et al. 2013). At microwave wavelengths, this cluster is a bright Sunyaev–Zeldovich effect source (Mroczkowski et al. 2012) which has enabled an estimate of its radial velocity through the Doppler shift induced by the plasma in the cluster to the photons of the cosmic microwave background (Sayers et al. 2013). In the optical, a filament of galaxies seems to extend over cosmic scales from the centre of this cluster (Ebeling, Barrett & Donovan 2004; Medezinski et al. 2013). The same filament can be observed in weak lensing maps (Jauzac et al. 2012; Medezinski et al. 2013) confirming that this cluster represents a 'node' of the cosmic web. Strong gravitational lensing has uncovered a complex structure where the distribution of lensed images is more anatomical in shape than it is geometrical (Z09) so that the strong lensing was not recognized for years despite adequate

★E-mail: jdiego@ifca.unican.es
†Hubble Fellow.

archival data. Several subclusters may be converging to form one of the largest, complex and most extreme clusters in the Universe (Z09; Jauzac et al. 2012; Limousin et al. 2012; Mroczkowski et al. 2012). According to Z09, this cluster is the largest lens known to date, with an effective Einstein radius of ≈55 arcsec (note however that MACS0717 has a smaller surface area within the caustics than, for instance Abell 1689.)

The extreme nature of this cluster is better appreciated in X-rays where the plasma temperature may exceed 20 keV in some places (Ma, Ebeling & Barrett 2009). The high-temperature regions observed in X-rays correlate well with shocks that are detected in radio maps (Bonafede et al. 2009; Pandey-Pommier et al. 2013). Radio observations have also confirmed that the radio emission is polarized, indicating that the magnetic field is ordered on large scales. The alignment of the radio halo perpendicular to the long axis of the DM distribution suggests that the radio emission is the result of a merger-related shock wave, with the emitting particles being shock accelerated (van Weeren et al. 2009). The SZ effect is well mapped in this central region with high-resolution Mustang data (Mroczkowski et al. 2012) confirming the pressure enhanced shocked gas and they find a high line-of-sight velocity for a central gas component of $+3600\,\mathrm{km\,s^{-1}}$, from a claimed detection of the Kinetic SZ effect, in agreement with the internal galaxy velocity analysis of Ma et al. (2009), and nearly orthogonal to the long axis of the DM, implying multiple merging.

In this paper, we use the recently released data from the Hubble Frontier Fields programme[1] (or HFF hereafter) on this cluster. We identify new multiply imaged systems that are later used to constrain the mass model of this cluster with an unprecedented number of constraints. We apply our robust free-form reconstruction method that does not rely on major assumptions about the distribution of DM other than the safe assumption that the galaxy members contain some mass and that more luminous galaxies correspond in general to more massive galaxies.

The paper is organized as follows. We describe the Hubble data in Section 2. The lensing data is described in Section 3. In Section 4, we give a brief description of the reconstruction method. Section 5 presents the results of the lensing analysis. The robustness of our solution is discussed in more detail in Section 6. We discuss our results in Section 7, and finally we conclude in Section 8.

Throughout the paper, we assume a cosmological model with $\Omega_{\mathrm{M}} = 0.3$, $\Lambda = 0.7$, $h = 70\,\mathrm{km\,s^{-1}\,Mpc^{-1}}$. For this model, 1 arcsec equals 6.46 kpc at the distance of the cluster.

2 HFF DATA

In this paper, we used public imaging data obtained from the ACS (filters: *F*435*W*, *F*606*W* and *F*814*W*) and the WFC3 (*F*105*W*, *F*125*W*, *F*140*W* and *F*160*W*), retrieved from the Mikulski Archive for Space Telescope (MAST). The data used in this paper consists of ≈1/3 of the data to be collected. Part of the data comes from CLASH (Postman et al. 2012). This release includes the first 40 orbits of observations of MACS0717 from the Frontier Fields programme ID 13498 (PI: J. Lotz), also including archival ACS and WFC3/IR data (programmes 9722 and 10420, PI.: H. Ebeling; programmes 10493 and 10793, PI.: A. Gal-Yam; programme 12103, PI.: M. Postman; programme 13389, PI.: B.Siana; and programme 13459, PI.: T. Treu). Previous observations from earlier shallow imaging (14 orbits in total) are also included in the release, together with the 40 orbits from the HFF campaign. The current release contains 15 orbits in the band *F*435*W*, 1 orbit in the band *F*606*W*, 30 orbits in the band *F*814*W* and eight orbits in the WFC3 infrared (IR) bands. The relatively low number of orbits in the IR bands makes the current release not ideal for detecting high redshift objects but the deep band at *F*814*W* allows us to reliably detect intermediate redshift candidates. In the IR bands, we use the background corrected images, corrected for a time-dependent increase in the background sky level (see for instance Koekemoer et al. 2013). In the optical bands, we use the self-calibrated images with improved low-level noise.

From the original files, we produce two sets of colour images combining the optical and IR bands. The first set is based on the raw data while in the second set we apply a low-pass filter to reduce the diffuse emission form member galaxies. The second set is particularly useful to match colours in objects that lie behind a luminous member galaxy.

3 LENSING DATA

Our starting set of strong lensing data is primarily based on the system identification of Z09. Some systems in Z09 are updated with new spectroscopic redshifts from Limousin et al. (2012), Schmidt et al. (2014) and Vanzella et al. (2014), and also some system definitions are improved following Limousin et al. (2012), Medezinski et al. (2013) and Richard et al. (2014). System 2 was excluded in some previous analyses since this source was too faint. The new and much deeper HFF data confirms this system as a reliable one so we include it in our analysis. Using this set of systems we build a lens-model that is later used to find new candidates taking advantage of the deeper Hubble observations. Many system candidates can be found in the new data set. In this paper, however, we rely only on the most robust subsample. This robust subsample is defined after we require that the system candidates must have similar colours and morphological features. Also, these systems must be consistent in terms of location in the lens plane and parity with the lens model derived in our first step. In the process of identifying new candidates, we need to assume a redshift for the systems. The lower number of orbits of the IR bands and the *V* band (*F*606*W*) compared with the *F*814*W* band does not allow for precise photometric redshifts of faint objects. Redshifts predicted by the lens models have demonstrated its usefulness and can be competitive with photometric redshifts as shown in Lam et al. (2014). This is particularly true for clusters with shallow mass profiles (like MACS0717) where the shallow mass distribution makes the location of image pairs extraordinarily sensitive to their redshift. We identify 17[2] new multiple systems that roughly double the original 16 systems in Z09, Limousin et al. (2012) and Richard et al. (2014). In addition to the new multiple systems, we include also 10 elongated arclets (with no identified counter-image) that are helpful to constrain the mass distribution around the critical curves and beyond the Einstein radius. The inclusion of the elongated arclets in our lens model are useful since they incorporate important information about the magnification. This is of particular interest in the regions beyond the

[1] http://www.stsci.edu/hst/campaigns/frontier-fields/

[2] At the time of submission of this paper new optical data released through the MAST archive has allowed us to uncover 13 system candidates in addition to the 17 new systems used in this work. These 13 new systems have not been used in this paper but are included in Table A2 in the appendix for completeness. Stamps of these new systems are also provided in the website http://www.ifca.unican.es/users/jdiego/MACS0717.

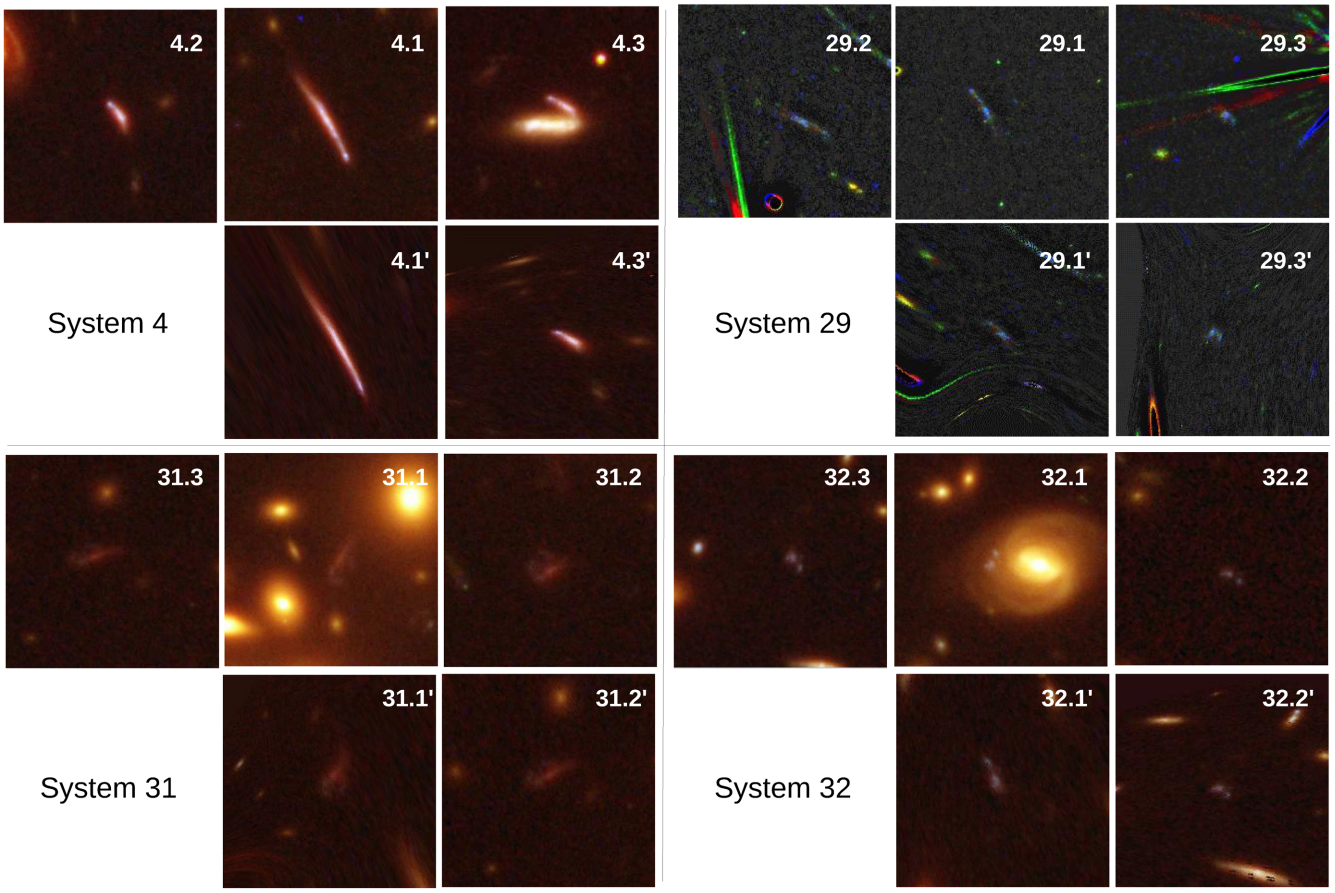

Figure 1. Examples of lensed systems compared with the prediction from our model. We show four systems. For each case, the top row contains three counter-images, with the first one on the left being used to predict the lensed counter-images (bottom) for which the predicted details are readily recognized in these cases. Each stamp corresponds to 6.6 arcsec across.

Einstein radius where the lensing constraints from multiply lensed images disappear. As described in our earlier work (Diego et al. 2005a,b, 2007, 2015b), the elongated arcs are incorporated into our method through their extent. The reconstruction algorithm uses this information to constrain the mass that *focuses* each arc into a small region at the desired redshift. These arcs are selected after checking a lens model that is based on a smaller subset of arcs. Using this model, we identify regions in the lens plane where elongated arcs are expected for background reshifts 2 or 3. We select those arcs that are found in the previously identified regions and that have the orientation predicted by the model and a colour consistent with the redshift.

We include the recently confirmed (spectroscopically) system at $z = 6.387$ as system 19 (following Richard et al. 2014 notation). Our model makes a clear prediction for a third image for this system but it could not be found with the current data. Also, the magnification for the third image is predicted to be significantly smaller ($\mu \approx 2$) than for the other two images. We should note that in previous works, the original system 19 was considered by other authors as part of our system 18 at $z = 2.4$ but the new system 19 at $z = 6.387$ is completely different (and already used in Richard et al. 2014). Also, a third counter-image 19.3 is proposed in Richard et al. (2014), very close to our predicted position. However, several faint sources can be seen in that area. The HFF cannot confirm nor reject this candidate as it is very faint. Hence, we do not use the candidate 19.3 from Richard et al. (2014) in our analysis. More arclets can be identified in the new Hubble images that will be incorporated in future works together with some of the candidates not used in this work and that are expected to be confirmed with the future Hubble data. Our complete strong lensing data set is listed in Table A1 in the appendix. Colour stamps of the full data set can be found in the website described in footnote 2.

A few examples[3] showing re-lensed images involving the previously known system 4 and the new systems 29, 31 and 32 are shown in Fig. 1. In general, we find a very good agreement between the re-lensed systems and the observed ones. In some cases, differences form the observed arcs highlight deficiencies in our lens model. For instance, the relensed system 32.1 arcmin in Fig. 1 differs in orientation and magnification from the observed one (32.1). In this case, the spiral galaxy shown in the stamp 32.1 is not included in our lens model that only includes elliptical galaxies. As shown by Diego et al. (2015a), this system could be used effectively to constrain the mass profile of the spiral galaxy, which is acting as a secondary lens.

The relative positions of the images defining our lensing data set is shown in Fig. 3. Fig. 2 shows examples of model predictions for three systems. The grey regions represent the distances (in the source plane but translated into the image plane) between the model

[3] See http://www.ifca.unican.es/users/jdiego/MACS0717 for more examples.

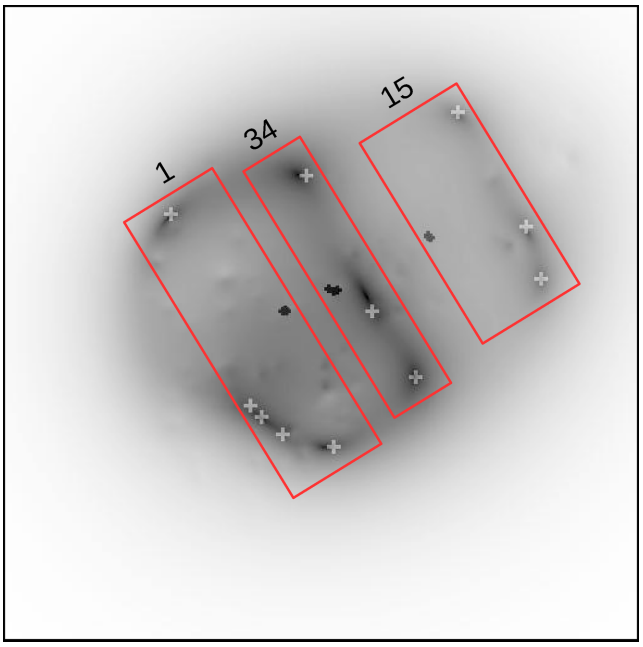

Figure 2. Examples of model predictions for systems 1, 15 and 34. Light grey crosses mark the position of the observed arcs. Darker regions mark the predicted position in the image plane of the arcs from our lens model. Dark crosses mark the predicted position of the observed arcs in the source plane.

prediction and the position of the source (this position is also part of our solution, or array X, described below in Section 4). The darker the region the more likely a lensed image is to be observed at that position. The positions of the observed arcs are marked with light grey crosses while the position of the observed arcs projected back into the source plane are marked with dark crosses. Based on our model predictions, colour information, morphology of the galaxies and model-based parity, we are able to identify all the additional multiple images listed in the appendix. The model predictions are useful to identify possible problems with the system identifications like in system 34 in Fig. 2. The position of the arcs in the source plane do not agree as well as in the other systems highlighting a possible problem with our lens model in this particular region of the cluster or that the redshift of this system may need to be revised. The new HFF data will help clarify some of these systems and also allow for a firmer identification of other system candidates not used in this work. The model predictions for all the systems can be found in the website[4] with the support material. These model predictions show also the expected position of the counter-images that could not be identified with the current data. Some of these counter-images are predicted to be demagnified versions of the background galaxies buried in the cluster members and hence very unlikely to be uncovered.

Fig. 3 shows the full data set together with the critical curve for one of our models (case IV described below in Section 4.1).

Although we are confident about our new system identification (they all are consistent with the lens model and show similar colours), it is possible that some corrections are made when the future data arrives (we should remind that we are using 1/3 of the planned data), specially for the unresolved galaxies for which the lack of morphological information does not allow for a more firm confirmation. We should however highlight that since these systems are consistent with the lens model, even in the situation where a few systems are wrongly matched, we do not expect significant changes in or lens model and/or conclusions in this work.

[4] Additional examples can be found in this website http://www.ifca.unican.es/users/jdiego/MACS0717

4 RECONSTRUCTION METHOD

We use the method, WSLAP+, to perform the mass reconstruction. The reader can find the details of the method in our previous papers (Diego et al. 2005a,b, 2007, 2015b,c; Ponente & Diego 2011; Lam et al. 2014; Sendra et al. 2014). Here, we give a brief summary of the most essential elements.

Given the standard lens equation,

$$\beta = \theta - \alpha(\theta, \Sigma), \tag{1}$$

where θ is the observed position of the source, α is the deflection angle, $\Sigma(\theta)$ is the surface mass density of the cluster at the position θ, and β is the position of the background source. Both the strong lensing and weak lensing observables can be expressed in terms of derivatives of the lensing potential,

$$\psi(\theta) = \frac{4\,G D_{\rm l} D_{\rm ls}}{c^2 D_{\rm s}} \int d^2\theta' \Sigma(\theta') ln(|\theta - \theta'|), \tag{2}$$

where $D_{\rm l}$, $D_{\rm s}$, and $D_{\rm ls}$ are the angular diameter distances to the lens, to the source and from the lens to the source, respectively. The unknowns of the lensing problem are in general the surface mass density and the positions of the background sources. As shown in Diego et al. (2005a), the strong lensing problem can be expressed as a system of linear equations that can be represented in a compact form,

$$\Theta = \Gamma X, \tag{3}$$

where the measured strong lensing observables are contained in the array Θ of dimension $N_\Theta = 2N_{\rm SL}$, the unknown surface mass density and source positions are in the array X of dimension $N_X = N_{\rm c} + N_{\rm g} + 2N_{\rm s}$ and the matrix Γ is known (for a given grid configuration and fiducial galaxy deflection field) and has dimension $N_\Theta \times N_X$. $N_{\rm SL}$ is the number of strong lensing observables (each one contributing with two constraints, x, and y), $N_{\rm c}$ is the number of grid points (or cells) that we use to divide the field of view. In this paper, we consider a regular grid of $N_{\rm c} = 32 \times 32 = 1024$ cells covering the field of view shown in Fig. 3 (4 arcmin). Each grid point contains a Gaussian function. The width of the Gaussians are chosen in such a way that two neighbouring grid points with the same amplitude produce a horizontal plateau in between the two overlapping Gaussians. $N_{\rm g}$ is the number of deflection fields (from cluster members) that we consider. In this work, we test two different configurations for the deflection field where $N_{\rm g}$ is equal to 2 (all member galaxies conform a unique deflection field except one foreground galaxy that is placed in a different redshift) or $N_{\rm g} = 5$ which corresponds to the case where some bright galaxies are treated in an independent way from the rest of the cluster members. Details of these two configurations are given in the next subsection. $N_{\rm s}$ is the number of background sources (each contributes with two unknowns, β_x, and β_y). The solution is found after minimizing a quadratic function that estimates the solution of the system of equations (3). For this minimization, we use a quadratic algorithm which is optimized for solutions with the constraint that the solution, X, must be positive. Since the vector X contains the grid masses, the re-normalization factors for the galaxy deflection field and the background source positions, and all these quantities are always positive

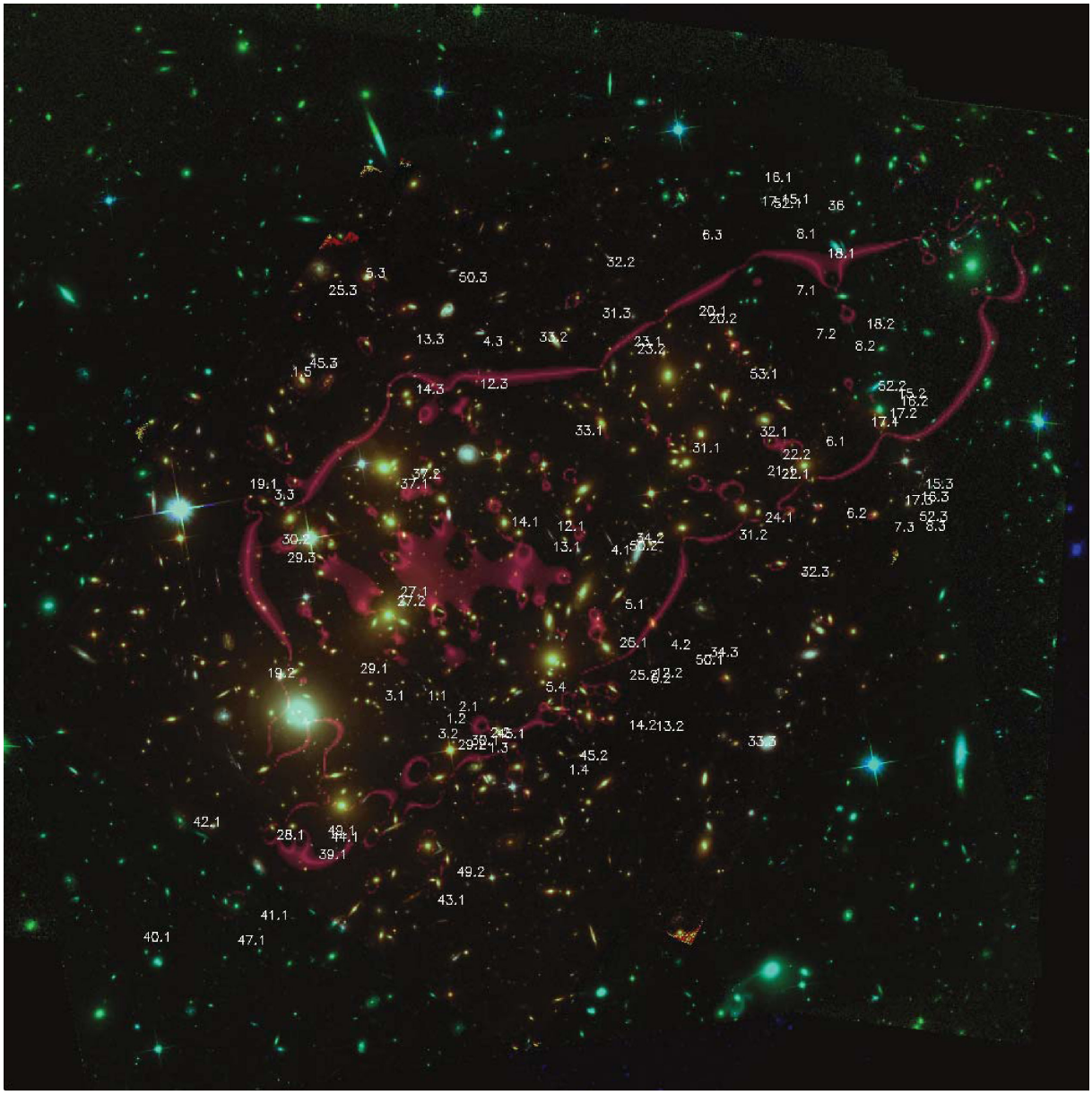

Figure 3. Compilation of systems used in the reconstruction and presented in the appendix. The critical curve ($z_s = 3$) for model IV described in Section 4.1 is shown superimposed in fuchsia ($z_s = 3$) The field of view is 4×4 arcmin^2 and north is up.

(the zero of the source positions is defined in the bottom-left corner of the field of view), imposing $X > 0$ helps in constraining the space of meaningful solutions. The condition $X > 0$ also helps in regularizing the solution as it avoids large negative and positive contiguous fluctuations.

4.1 Member galaxy deflections

The member galaxies defining our fiducial galaxy field are all elliptical galaxies selected from the red sequence (based on the *Hubble Space Telescope – HST* near-IR bands from 1 to 1.6 μm). The most luminous galaxy in the Hubble image is a known foreground galaxy (2MASX J07173724+3744224) at $z = 0.1546$ (Pandey-Pommier et al. 2013). This galaxy, although well in the foreground is still relatively luminous and hence its mass may have a non-negligible effect in the lens model. Following Z09, we include this galaxy in our lens model but set this galaxy to be at $z = 0.1546$. The remaining galaxies in the cluster are assigned a fiducial mass based on their flux. Given the galaxy member positions and masses, M_i, we assume an NFW profile for each galaxy with a scale radius proportional to $M_i^{1/3}$. A fiducial deflection field is then computed summed from these galaxy members, as their deflections add linearly via the lensing equation. The galaxies are 'split' into different layers to account for possible projection effects and/or some variation in the galaxy luminosity-to-mass ratio. Our method re-scales this fiducial field by a constant C per layer and combines it with the fiducial field from a gridded mass distribution to reproduce the observed positions and magnifications of the multiply lensed systems and arclets. For clarity, the layers used in this work are explicitly shown in Fig. 4 and these additional normalization parameters are accounted for when calculating the chi-square fit to the data. In the same plot, we also indicate the galaxies that conform the different layers. We

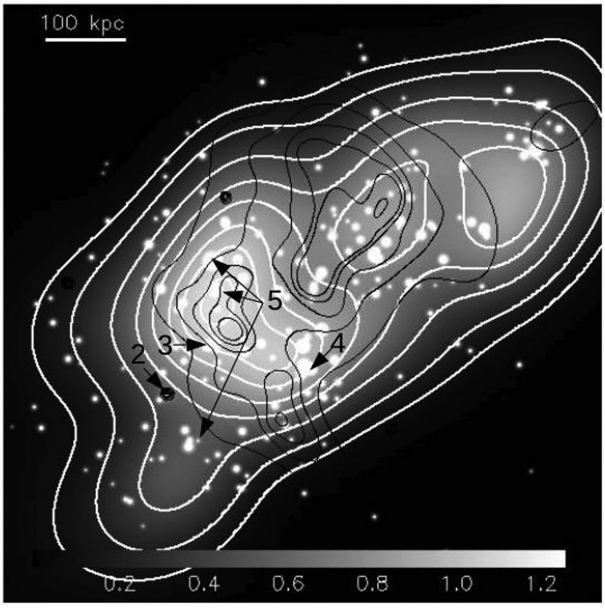

Figure 4. Reconstructed mass in MACSJ0717 in units of its convergence, κ, for $z_s = 3$. This solution corresponds to case IV described above. The other cases look very similar. The convergence maps have been saturated beyond $k = 1.25$ for clarity purposes. The white contours corresponds to $\kappa = 0.1, 0.2, 0.4, 0.6, 0.75, 0.9, 1.0, 1.1, 1.15$, respectively. The last level overlaps with the saturation level so it cannot be appreciated in this plot. The black contours represent the X-ray data from *Chandra*. X-rays have been smoothed with ASMOOTH (Ebeling, White & Rangarajan 2006). The numbers show the galaxies which belong to each layer (2–5). The galaxies that are not marked belong to layer 1.

explore four different solutions according to the number of layers used in the reconstruction and/or the number of iterations in the minimization process.

(I) This is the simplest model with two layers for the fiducial field of galaxies. Layer one contains all the galaxy cluster members at $z = 0.546$ and layer 2 contains the foreground galaxy at $z = 0.1546$. The solution is obtained after 5000 iterations of the code. This range of iterations was proven in earlier works to be a safe number to avoid overfitting.

(II) As in case I above but we double the number of iterations to 10 000. In most cases, at this regime signs of overfitting start to be evident in the solution like oversized radial critical curves. However, at 10 000 iterations these signs are still not present in the solution.

(III) As in case I (5000 iterations) but considering five layers instead of two. Like in case I layer 2 contains the foreground galaxy at $z = 0.1546$, layer 3 contains a big elliptical galaxy at its centre, layer 4 contains another large galaxy south-west of the central galaxy, layer 5 contains three large galaxies, two above and one below the central galaxy. Finally layer 1 contains all the remaining galaxies (these galaxies are shown explicitly in Fig. 8 below).

(IV) As in case III but for 10 000 iterations.

We should note that in all these cases we make the *wrong* assumption that the mass associated with the galaxies is circularly symmetric. By doing this, we neglect the fact that all galaxies have some degree of ellipticity. However, as shown in a previous work (Diego et al. 2015c) the impact of this assumption is small and it is important only in those cases where an arclet is close to a massive galaxy cluster member. Some of the larger errors listed in Table A1 could be due for instance to this assumption.

5 DM DISTRIBUTION

The mass reconstruction is shown in Fig. 4 for the solution obtained in case IV discussed in the previous section. Together with the mass, we show the X-ray emission from *Chandra*. The *Chandra* data has been smoothed using the widely used code ASMOOTH (Ebeling et al. 2006). The solutions for the other three cases are shown in Fig. 5. The contours in Figs 4 and 5 correspond to the *smooth* component of the mass distribution obtained after subtracting the galaxy contribution to the mass map from the total mass. The first conclusion we can derive from these results is that the mass distribution shows multiple distinct concentrations as shown in Figs 4 and 5. Earlier work has generally claimed four peaks in this region (Ma et al. 2009; Limousin et al. 2012; Medezinski et al. 2013). A more precise picture of the location of our peaks can be seen in Fig. 9 below. Three of our detected maxima correlate well with the observed galaxy and gas enhancements as seen in Fig. 9. The third peak on the right-hand side of the image (west) shows a significant offset both with the galaxies and X-rays. Some caution should be exercised with regard to this third peak as we observe have no lensing constraints to help beyond this peak. This subgroup of galaxies does coincide with an X-ray emission peak whereas our mass peak does not, so this is intriguing but certainly would benefit from more clarification. The quality of the Hubble data at the position of this subgroup is significantly poorer than in the rest of the cluster, making it more to identify lensed images in this area but better data to come from the HFF should help in the near future.

A direct comparison of the four solutions discussed in the previous section is shown in Fig. 6. The agreement between our four cases is very clear, indicating that our solution is robust against the assumptions made about the fiducial galaxies or the number of iterations. The same plot shows the comparison with the smoothed X-ray data. In X-rays, several prominent point sources match sources in the HFF data. In Fig. 6, we label some of them (only some relevant X-ray sources are marked in this figure). All the X-ray point sources except one, have a clear counterpart in the HFF field of view. The only exception is source X4 in Fig. 6. At approximately 1 arcsec separation, we find a small group of three very faint objects where one of them may be the source of the X-ray emission. Deep follow-up observations at different wavelengths at this position may reveal an interesting object (like a magnetar). The source labelled X1 corresponds to the foreground galaxy at $z = 0.1546$. Radio observations reveal that this source either hosts two very powerful radio jets (more likely) or it lies in front of an unusually straight shock front in the cluster (van Weeren et al. 2009, less likely). In X-rays, the foreground galaxy shows up as a powerful X-ray source, possibly hosting a supermassive black hole at its centre, a picture that is in agreement with the observed flattening of the light profile in the centre. This flattening is expected when a supermassive black hole is at the centre of a galaxy (Postman et al. 2012; Rusli et al. 2013; Lopez-Cruz et al. 2014; Thomas et al. 2014). Sources X2 and X3 are interesting from the lens model point of view. If we assume that X2 is at redshift $z = 5$, our model predicts that we should expect a counter-image within a few arcseconds of source X3. In the optical, both X2 and X3 share a rather similar morphology with a nucleus surrounded by dusty arms. However in terms of galaxy size, lens magnification and relative orientation, the hypothesis that galaxies X2 and X3 are in fact the same object, loses support. Also, in terms of colour galaxy X2 appears significantly redder than galaxy X3.

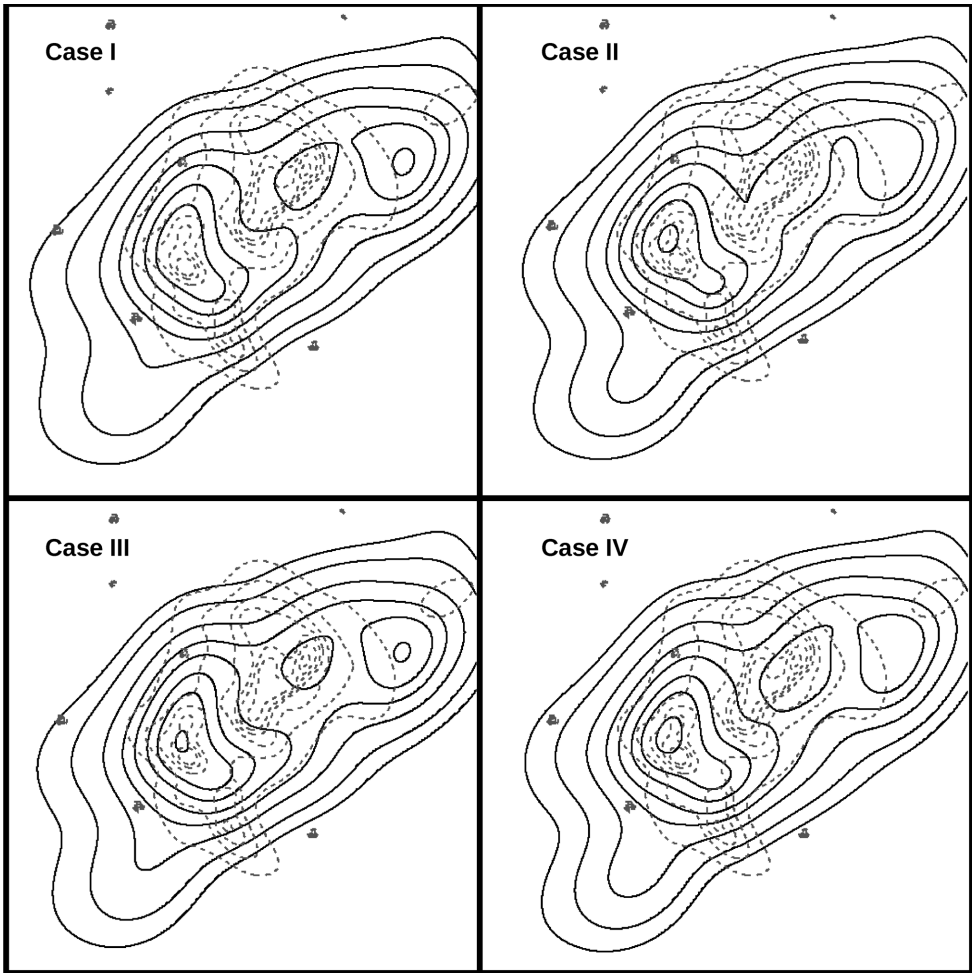

Figure 5. Like in Fig. 4 but comparing the DM to the X-ray contours for the four different solutions. The DM component corresponds to the total mass map minus the galaxy component. The compact grey sources are X-ray sources (see the text).

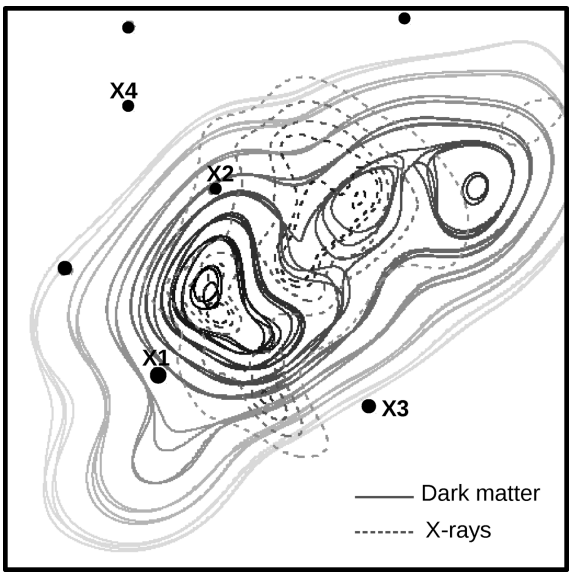

Figure 6. Like in Fig. 5 but comparing the four solutions for the DM distribution (solid contours) with the X-ray distribution from *Chandra* (dashed contours) shown for comparison. The points X1, X2, X3, and X4 mark the position of selected bright X-ray sources (see the text).

The profile of the mass model is presented in Fig. 7. Due to the lack of symmetry of this cluster, the definition, and interpretation of the profile is more challenging than in more relaxed and rounded clusters. In an attempt to capture some of the symmetry of the central DM peak, the centre of the profile in Fig. 7 is defined at the position of the most massive galaxy that is closest to centre of the most massive peak in our reconstructed mass. This corresponds to group C (see Fig. 9 below) as defined by (Ma et al. 2009, and again in Limousin et al. 2012). More specifically, the centre is taken at RA = 07:17:35.534, Dec. = +37:45:0515 (J2000). As found in Ma et al. (2009), and later in Limousin et al. (2012), we find that group C is also the most massive. We show the profile of the total mass (dashed) and the grid component after subtraction of the contribution from the galaxies. The profile is strikingly shallow up to a 100 kpc, confirming earlier findings based on parametric methods Z09, Limousin et al. (2012) and Medezinski et al. (2013). In previous analyses based on data of two other HFF clusters, A2744 and MACS0416, we found also very shallow profiles in the central region (Lam et al. 2014; Diego et al. 2015c) in agreement with results from other authors. The fact that these shallow profiles seem to appear in merging clusters may point in the direction that the shallowness is a consequence of the superposition of smaller haloes in the central region. This, however, does not explain why there are not visible cusps associated with the individual haloes, and in particular

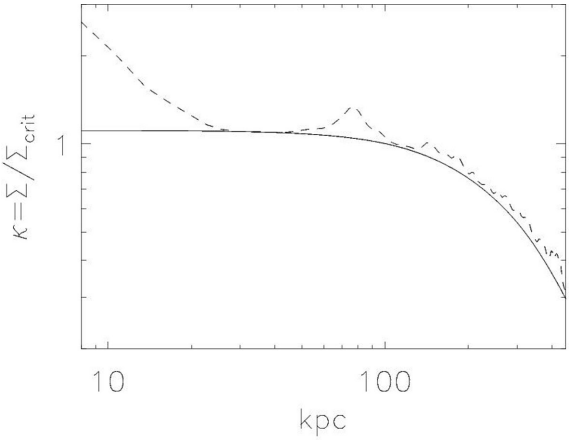

Figure 7. Profile of the solution for case IV. The mass is presented in terms of the critical surface mass density, computed for $z = 3$ to match the mean background redshift. The dashed line shows the total mass of galaxies plus the free-form grid and the solid line is for the grid alone corresponding to the 'soft' cluster-wide mass distribution. The profile is centred in the massive galaxy member that is closer to the centre of peak C in Fig. 9 below.

in the dominant halo in group C. Cusps are expected to survive after a cluster merger. In Diego et al. (2015c), we discuss some additional possible explanations, these include mechanisms related to the baryonic component like feedback or scouring by supermassive black holes that are predicted to flatten the very central part of the galaxies they host. These mechanisms are however unlikely to have a significant impact on scales of tens of kpc. An interesting alternative discussed in the context of another HFF cluster in Diego et al. (2015c) is the possibility that DM has a small, but not negligible, probability of interaction. Simulations have shown that this mechanism, if present, is able to flatten the cusps of cluster haloes and on the necessary scales up to 100 kpc (Rocha et al. 2013). In addition to the flattening, if DM interacts, it should exhibit a friction effect that could in principle be studied by possible shifts between the peaks of the DM distribution and the galaxies. To explore in this direction further it is necessary to increase the number of multiple images in the central regions of the cluster in order to constrain better the mass distribution. The future HFF data in this cluster may reveal enough strong lensing information to address the questions arising from our comparison more definitively.

In terms of integrated total mass of our models, we find $M_{\rm tot} = 1.27(\pm 0.21) \times 10^{15}\,{\rm M}_{\odot}$. However, we should not that our model is largely insensitive to the mass beyond the lensing constraints where our lens model is known to be biased towards lower masses (see Sendra et al. 2014 and references therein) so this mass should be interpreted as the integrated mass within the region defined by the lensing constraints. More meaningful is the total mass associated with the compact galaxy component. We find $M_{\rm gal} = 1.1(\pm 0.17) \times 10^{14}\,{\rm M}_{\odot}$. In both cases, the errors correspond to the dispersion of the models I, II, III and IV described in the previous section.

6 VARIABILITY OF THE SOLUTION

The motivation to produce the different solutions in cases I, II, III and IV is to study the variability of the solution with respect to our input galaxies. As discussed in earlier works, the solution is not unique and an infinite number of models are equally consistent with the data. Typically, the more constraints used in the reconstruction the more similar all these infinite models are. In Fig. 6, a preliminary comparison of the variability of the solution was presented. The four solutions agree very well in general but also with some small differences that we investigate in more detail in this section. In Fig. 8, we show the dispersion of the four solutions normalized to the mean of the solutions and multiplied by a factor 100 to represent percentages. The largest variation in the solutions occurs in the south-east sector of the cluster. By looking at the individual differences,[5] we check that the variability in this part of the lens is larger when comparing cases I-II, and I-III (see Fig. A1 in the appendix). That is, this variability is mostly due to the increase in the number of iterations. This is not surprising since in this region we find the largest concentration of individual arclets (without counterparts). These constraints, although useful, are weaker than the constraints coming from multiply lensed galaxies. Hence, they become more relevant only at the end of the minimization process. In general, the largest differences concentrate in the region where the lensing constraints disappear.

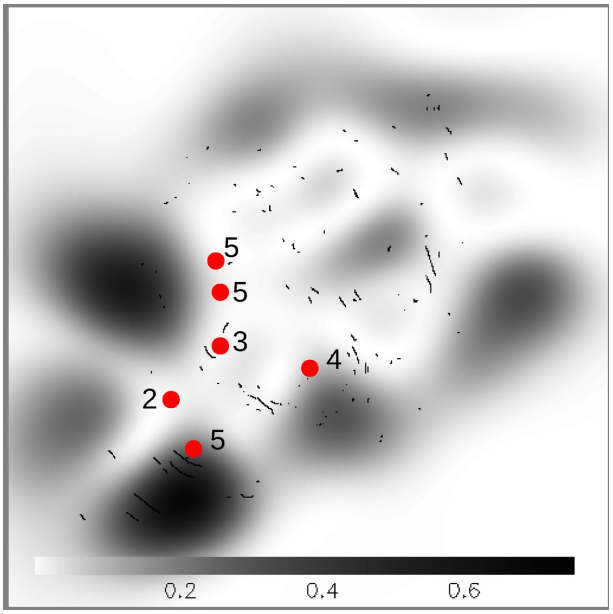

Figure 8. Normalized dispersion of the diffuse component of the solutions (in percent). The full data set used to do the reconstruction is also shown. The larger variations in the solution concentrate around the areas where the lensing constraints start to disappear or where the single arclets (shown in black) start to become important. The red discs mark the positions of the galaxies whose amplitudes are adjusted independently (cases III and IV). The number next to the galaxy indicates the layer in which the galaxy is placed. The foreground galaxy corresponds to layer number 2. All remaining member galaxies not shown in this plot are placed in layer 1.

Also related with the variability in the solutions, we compute the difference between the predicted position of the counter-images and the observed positions. This difference can be seen as an error associated with the lens models and identifies also the regions in the image plane where the model is less precise. We compute this error for each one of the four cases described above and compute the mean and dispersion of the derived four values for each counter-image. The result is shown in column 4 of Tables A1 and A2 in the appendix. In general, we find that all four cases give relatively consistent results in terms of this error with a probability density

[5] The individual differences can be found in http://www.ifca.unican.es/users/jdiego/MACS0717

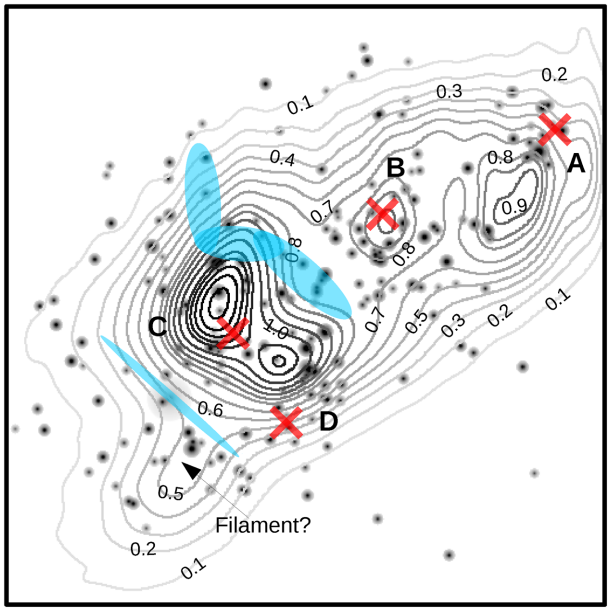

Figure 9. Higher resolution version of the soft, free-form cluster component of the mass map obtained after a partial deconvolution. Those galaxies included in our model as small perturbations, are also shown for comparison. The contour levels are for κ at $z = 3$. The contour levels between $\kappa = 0.8$ and 1.05 increase in intervals of $\Delta\kappa = 0.05$. The contour levels above $\kappa = 1.05$ increase in intervals of $\Delta\kappa = 0.025$. The highest level corresponds to $\kappa = 1.125$. The X symbols mark the position of the four X-ray peaks. The labels A,B,C,D denote the four subgroups seen in the optical (Ma et al. 2009). The blue semitransparent regions mark the approximate position and morphology of the radio emission (van Weeren et al. 2009).

function for the errors that is well described by a Gaussian with zero mean and dispersion ≈2.8 arcsec. More precisely, the dispersion of the errors is 2.5, 3.2, 2.7 and 2.8 arcsec for cases I, II, III and IV, respectively. Using the solutions from the four cases, we compute also the variability in the predicted (but not matched) positions listed in Table A3 in the appendix. These values are shown in the last column of Table A3. In this case, we do not compute the difference between observed and predicted positions as there is no candidate for the counter-image identified in the data. However, it is reasonable to expect an additional error of ≈2.8 arcsec due to the intrinsic error of the individual lens models.

7 DISCUSSION

The galaxy cluster MACS0717 is one of the most interesting cases for examining the interplay between baryonic and DM. Multiwavelength observations of this cluster have revealed powerful radio haloes that trace shock regions. The shocks are probably produced by the near simultaneous merging of several large clusters. This merging geometry can, in principle, be understood better through observations of the kinetic Sunyaev–Zeldovich effect of the gas in the cluster as this is proportional to the velocity along the line of sight (Mroczkowski et al. 2012; Sayers et al. 2013). Analysis of X-ray data confirms the extreme nature of this cluster with temperatures in excess of 20 keV, making this cluster one of the hottest known so far. In terms of mass, this cluster lies in the top end of what is expected for standard models with its mass distribution extending well beyond the field of view covered by the HFF observation. Weak lensing analyses (Jauzac et al. 2012; Medezinski et al. 2013) reveal a filamentary structure towards the south-east from the centre and traced by the elongated galaxy distribution (Ebeling et al. 2004). The point where the filament meets the cluster can be seen in our lens model which shows an elongation in the south-east part of the cluster and responsible for the highly elongated lensed images we have used in our model.

Previous lensing work has been based on parametric methods (Limousin et al. 2012; Richard et al. 2014), where the central region of the cluster has been divided into four separate substructures, relying on the optical galaxy distribution. Interestingly the soft component of our mass model, where we have removed the galaxy mass contribution from the total mass also shows a distribution for which four density maxima may be reasonably defined (Figs 4, 5, and 6). This substructure is made more evident when we deconvolve partially the smooth component of our mass model. Since the smooth component is a superposition of a grid of Gaussians with a given 'pixel' scale, the resolution of the soft component is limited by the width chosen for the Gaussian. Ideally this grid should be fine enough to follow all relevant substructures, but a partial deconvolution highlights the internal structure of the mass distribution after deconvolution may be even more representative of the true underlying mass distribution. Fig. 9 shows the partially deconvolved version of the soft component of the mass distribution for case IV discussed above. When the deconvolved mass distribution is compared with the brightest galaxies from the cluster four components of the mass distribution are now more evident. The correspondence between the location of these galaxy peaks with the general soft mass distribution (after subtracting the member galaxies) is a striking and need not have turned out this way given the freedom of our grid based modelling. In the case of the group A, on the right-hand side of the HFF field at the apex of the strongly lensed region, we find a mass peak but we see that its centre does not coincide well with the subgroup of what appear to be member galaxies on the upper-right corner of the image. As discussed earlier, this could be the result of the lack of lensing constraints beyond that subgroup so certainly the reliability of this peak should not be considered as high as in the other three. Further HFF imaging may help clarify this possible interesting discrepancy. Interestingly, this offset is also found in Limousin et al. (2012) in their blind test analysis (where the mass is not assumed to trace light a priori) highlighting the need for models (like our free-form model) that do not necessarily trace light. Also in Limousin et al. (2012) they also consider a five-component model in their blind analysis that the authors claim does not improve the fit further. However, the location of one of their peaks agrees well with the elongation in the south-east part of our model. We should note that according to Ebeling et al. (2004), and later to Medezinski et al. (2013), a massive filament emerges from this direction of the cluster towards the south-east, in excellent agreement with our findings (see Fig. 9). Also, it is important to note that Limousin et al. (2012) did not include the arclets in the south-east sector that we used in our analysis, possibly explaining why their fit did not show a significant improvement in their model.

The combined information from radio (shocks), optical, lensing and X-rays emission is that it is not clear whether this cluster is in an early phase of merging or it has gone through several core passages already. The radio data shows a region with prominent emission between the B group and the two western peaks (C and D) where X-ray temperatures are also found to be higher. The position and geometry of the radio feature is shown in Fig. 9 in semitransparent light blue. This picture suggests that group B and groups (C, D) are falling towards each other. On the other hand, measurements of the radial velocity (Ma et al. 2009; Mroczkowski et al. 2012) suggest a

significant radial component so combining the radio relic with the velocity measurements it is more likely group B is moving at an angle close to, but not too much, the line of sight. The presence of an extended radio relic in the cluster suggests the system is post first core passage. The foreground galaxy at $z = 0.1546$ lies in the middle of another arc with a straight geometry. This radio emission is likely produced by the AGN at this galaxy and hence not related to the cluster but it could be also a shock front as suggested by van Weeren et al. (2009), although in the same work the authors consider this option as less likely. If this straight feature originates at the cluster instead of the AGN, this could be a fundamental clue to determine the dynamical state of this cluster and would add evidence towards the post-merger hypothesis. In X-rays, the clear offset between the X-ray and luminous (or mass) peaks in group D in Fig. 9 points to significant dynamical friction from an ongoing merging process. On the other hand, the excellent agreement between the X-ray and mass peaks in group B points to a relatively mild interaction in the past of this group with the cluster environment although a small offset is also expected if B is moving in a path close to the line of sight where projection effects would hide any possible offsets.

Determining the dynamical state of the cluster is important. If the cluster is in the early merging phase, the interpretation that the shallow central profile may be a signature of self-interacting DM may be more unrealistic since this mechanism to flatten central cusps are more efficient when clusters collide edge-on (and after first core passage; Rocha et al. 2013). Of course, this possibility cannot be ruled out if this cluster has gone through multiple mergers in the past. A confirmation of the position of the DM peak for group A may lead to important consequences to understand the interplay between baryons and DM.

8 CONCLUSIONS

We have derived a free-form solution to the latest HFF data for MACS0717 and in so doing doubled the number of multiple images known. We started by adding those systems initially uncovered by Z09 and later revised and/or measured in Limousin et al. (2012), Medezinski et al. (2013), Schmidt et al. (2014) and Richard et al. (2014). We then used this model and the new deeper images from the HFF programme to identify 17 new multiply lensed systems doubling the number of known systems. Our method is general so we can make use of pixel positions along the full length of the many faint extended arcs that are visible in the new HFF data. These arcs belong to images comprising multiple systems and also individual long images for which no counter images are expected or which remain unidentified. Using all this information we derive a new lens model. Our new model agrees reasonably well with previous models based on a smaller number of multiply lensed images. We confirm the existence of four main concentrations of DM in the central part of this cluster. These clumps are still clearly seen even after the contribution from the galaxies is subtracted indicating that the member galaxies must have extended cluster haloes around them. Three of the clumps correlate well with the luminous matter, but less so with the X-ray emission and one of the clumps seem to prefer an area where no significant galaxies (or X-rays) are observed. This, however, could be a systematic effect due to the lack of constraints on this part of the lens. Future data from the HFF programme on this cluster will help on improving the lens models even more and will open new opportunities to understand the interplay between baryonic and DM in this interesting cluster.

Perhaps the most puzzling result is the very good agreement between some of the peaks of the soft DM component and the peaks in the X-ray and luminous matter while other peaks (in particular A and to some degree D) show a significant offset. The highly disturbed nature of this cluster, the offsets observed in some of the groups between X-ray and mass, the elongated critical curve and the presence of prominent radio emission suggest a collision between the groups. An energetic collision between clusters is expected to produce significant offsets between the galaxies (or lensing mass maps) and the plasma, as recently revealed in our HFF analysis of MACS0416 where distinctive offsets indicate this cluster is observed just after first core passage. These offsets are present only in groups A and D. The lack of offsets in group B could be explained by projection effects if B is moving close to the line of sight. The lack of offsets in group C may be understood if C is the most massive group and is less affected by collisions with its larger gravitational field being able to hold on to its gas (X-rays) better that the other groups. The offset between X-ray and mass in group D could be understood if C is moving close to the plane of the sky and towards the centre of mass of the cluster. The offsets in group A are the most difficult to understand although a possible explanation could be the lack of lensing constraints that do not allow to identify the peak at the right position. This is not an unrealistic situation if we realize that strong lensing in this cluster has long been unrecognized in the past despite being the largest gravitational lens known so far Z09.

We also confirm the shallowness of the mass profile. The earlier analysis by Z09 initially found it was very shallow and the largest known lens to date. The shallowness may be due, at least partially, to the accumulated effect of the four groups merging into a single massive cluster but could also be an indication of interesting physics related to the properties of DM. Detailed simulations of large mergers that incorporate a degree of viscosity in DM may be able to reproduce this degree of shallowness that is known to be present as well in the other HFF clusters analysed so far Lam et al. (2014) and Diego et al. (2015c). New data from the HFF programme on this cluster will also help improve the lens models even more, offering new opportunities to understand the interplay between baryonic and DM in this interesting cluster.

ACKNOWLEDGEMENTS

This work is based on observations made with the NASA/ESA *HST* and operated by the Association of Universities for Research in Astronomy, Inc. under NASA contract NAS 5-2655. The authors would like to thank the HFF team (lead by Jennifer Lotz and Matt Mountain) for making the data for this work available to the community. We thank The Frontier Fields Science Data Products Team (lead Anton M. Koekemoer) for gathering and compiling the HFF data base for this project. The scientific results reported in this article are based in part on data obtained from the Chandra Data Archive.[6,7,8] We would like to thank Harald Ebeling for making the code ASMOOTH (Ebeling et al. 2006) available. TJB thanks the University of Hong Kong for generous hospitality. JMD acknowledges support of the consolider project CSD2010-00064 and AYA2012-39475-C02-01 funded by the Ministerio de Economia y Competitividad. AZ was provided by NASA through Hubble

[6] ivo://ADS/Sa.CXO#obs/16305
[7] ivo://ADS/Sa.CXO#obs/04200
[8] ivo://ADS/Sa.CXO#obs/01655

Fellowship grant #HST-HF2-51334.001-A awarded by STScI. The authors thank Francisco Carrera, Nanda Rea and Marceau Limousin for very useful comments. We would also like to thank the anonymous referee for the suggestions that helped improve this paper.

REFERENCES

Akerib D. S. et al., 2014, Phys. Rev. Lett., 112, 091303
Bonafede A. et al., 2009, A&A, 503, 707
Diego J. M., Protopapas P., Sandvik H. B., Tegmark M., 2005a, MNRAS, 360, 477
Diego J. M., Sandvik H. B., Protopapas P., Tegmark M., Benítez N., Broadhurst T., 2005b, MNRAS, 362, 1247
Diego J. M., Tegmark M., Protopapas P., Sandvik H. B., 2007, MNRAS, 375, 958
Diego J. M., Broadhurst T., Benitez N., Lim J., Lam D., 2015a, MNRAS, 449, 588
Diego J. M. et al., 2015b, MNRAS, 446, 683
Diego J. M., Broadhurst T., Molnar S. M., Lam D., Lim J., 2015c, MNRAS, 447, 3130
Ebeling H., Barrett E., Donovan D., 2004, ApJ, 609, L49
Ebeling H., White D. A., Rangarajan F. V. N., 2006, MNRAS, 368, 65
Ebeling H., Barrett E., Donovan D., Ma C.-J., Edge A. C., van Speybroeck L., 2007, ApJ, 661, L33
Jauzac M. et al., 2012, MNRAS, 426, 3369
Koekemoer A. M. et al., 2013, ApJS, 209, 3
Lam D., Broadhurst T., Diego J. M., Lim J., Coe D., Ford H. C., Zheng W., 2014, ApJ, 797, 98
Limousin M. et al., 2012, A&A, 544, A71
Lopez-Cruz O., Anorve C., Birkinshaw M., Worrall D. M., Ibarra-Medel H. J., Torres-Papaqui J. P., Barkhouse W. A., Motta V., 2014, ApJ, 795, L31
Ma C.-J., Ebeling H., Barrett E., 2009, ApJ, 693, L56
Medezinski E. et al., 2013, ApJ, 777, 43
Mroczkowski T. et al., 2012, ApJ, 761, 47
Pandey-Pommier M., Richard J., Combes F., Dwarakanath K. S., Guiderdoni B., Ferrari C., Sirothia S., Narasimha D., 2013, A&A, 557, A117
Ponente P. P., Diego J. M., 2011, A&A, 535, A119
Postman M. et al., 2012, ApJS, 199, 25
Richard J. et al., 2014, MNRAS, 444, 268
Rocha M., Peter A. H. G., Bullock J. S., Kaplinghat M., Garrison-Kimmel S., Oñorbe J., Moustakas L. A., 2013, MNRAS, 430, 81
Rusli S. P., Erwin P., Saglia R. P., Thomas J., Fabricius M., Bender R., Nowak N., 2013, AJ, 146, 160
Sayers J. et al., 2013, ApJ, 778, 52
Schmidt K. B. et al., 2014, ApJ, 782, L36
Sendra I., Diego J. M., Broadhurst T., Lazkoz R., 2014, MNRAS, 437, 2642
Thomas J., Saglia R. P., Bender R., Erwin P., Fabricius M., 2014, ApJ, 782, 39
van Weeren R. J., Röttgering H. J. A., Brüggen M., Cohen A., 2009, A&A, 505, 991
Vanzella E. et al., 2014, ApJ, 783, L12
Zitrin A., Broadhurst T., Rephaeli Y., Sadeh S., 2009, ApJ, 707, L102

APPENDIX A: COMPILATION OF ARC POSITIONS

Table A1. Full lensing data set. The first column shows the system ID following the original notation of Z09. The second and third columns show the coordinates of each arclet. Column 4 includes the redshifts used in our study (taken from Z09 and Schmidt et al. 2014 when appropriate). Some of these redshifts are photometric and some are based on colour and/or predicted by the lens model. Column 5 (Error) shows the difference between the observed position and the predicted positions by the lens models (see Section 6). The last column contains additional useful information. New images used in the analysis are denoted with *N* in the *Notes* column. Spectroscopic redshifts are marked with an *S* in this column. The redshifts that are obtained from Z09 are denoted *Z*. When the redshifts come from Schmidt et al. (2014),we denote it with *Sc*. The system 19 confirmed by Vanzella at al. (2014) is denoted as *V*. Redshifts without a *S, Z, Sc* or *V* are photometric from Z09 or determined by the lens model *N*.

ID	RAJ2000 (h:m:s)	Dec.2000 (d:m:s)	z	Error (arcsec)	Notes
1.1	7:17:34.865	+37:44:28.39	2.963	6.15 ± 0.58	S,Z
1.2	7:17:34.514	+37:44:24.43	2.963	0.78 ± 0.22	S,Z
1.3	7:17:33.823	+37:44:17.88	2.963	10.20 ± 0.61	S,Z
1.4	7:17:32.234	+37:44:13.13	2.963	2.72 ± 1.05	S,Z
1.5	7:17:37.384	+37:45:40.95	2.963	2.86 ± 1.17	S,Z
2.1	7:17:34.267	+37:44:27.72	2.500	3.76 ± 0.60	
2.2	7:17:33.691	+37:44:21.30	2.500	4.67 ± 1.87	
3.1	7:17:35.645	+37:44:29.44	1.855	4.30 ± 2.09	S,Sc
3.2	7:17:34.656	+37:44:21.08	1.855	9.65 ± 3.45	S,Sc
3.3	7:17:37.702	+37:45:13.86	1.855	2.82 ± 0.02	S,Sc
4.1	7:17:31.440	+37:45:01.55	1.855	2.63 ± 1.65	S,Sc
4.2	7:17:30.324	+37:44:40.70	1.855	1.47 ± 0.26	S,Sc
4.3	7:17:33.828	+37:45:47.77	1.855	0.99 ± 0.33	S,Sc
5.1	7:17:31.169	+37:44:48.73	4.300	5.46 ± 0.75	
5.2	7:17:30.694	+37:44:34.19	4.300	2.33 ± 0.75	
5.3	7:17:36.000	+37:46:02.75	4.300	4.65 ± 0.60	
5.4	7:17:32.657	+37:44:31.33	4.300	1.11 ± 0.17	N
6.1	7:17:27.434	+37:45:25.56	2.100	2.15 ± 0.23	
6.2	7:17:27.041	+37:45:09.90	2.100	0.93 ± 0.00	
6.3	7:17:29.734	+37:46:11.21	2.100	0.85 ± 0.19	
7.1	7:17:27.970	+37:45:58.90	2.200	7.08 ± 0.32	
7.2	7:17:27.607	+37:45:50.87	2.200	1.87 ± 0.47	
7.3	7:17:26.160	+37:45:06.59	2.200	0.99 ± 0.33	
8.1	7:17:27.982	+37:46:10.81	2.300	4.10 ± 0.72	
8.2	7:17:26.890	+37:45:47.41	2.300	7.71 ± 0.43	
8.3	7:17:25.566	+37:45:06.88	2.300	1.79 ± 0.17	
12.1	7:17:32.438	+37:45:06.80	1.699	2.37 ± 0.02	S,Sc
12.2	7:17:30.617	+37:44:34.51	1.699	0.75 ± 0.28	S,Sc

Table A1 – *continued*

ID	RAJ2000 (h:m:s)	Dec.2000 (d:m:s)	z	Error (arcsec)	Notes
12.3	7:17:33.890	+37:45:38.38	1.699	9.68 ± 2.05	S,Sc
13.1	7:17:32.522	+37:45:02.30	2.547	1.98 ± 0.00	S,Z
13.2	7:17:30.610	+37:44:22.85	2.547	0.33 ± 0.33	S,Z
13.3	7:17:35.083	+37:45:48.20	2.547	1.40 ± 0.00	S,Z
14.1	7:17:33.305	+37:45:07.96	1.855	3.16 ± 1.08	S,Sc
14.2	7:17:31.111	+37:44:22.92	1.855	0.87 ± 0.33	S,Sc
14.3	7:17:35.076	+37:45:37.19	1.855	3.49 ± 1.22	S,Sc
15.1	7:17:28.253	+37:46:19.24	2.405	1.48 ± 0.00	S,Z
15.2	7:17:26.090	+37:45:36.29	2.405	2.04 ± 0.37	S,Z
15.3	7:17:25.584	+37:45:16.20	2.405	0.52 ± 0.08	S,Z
16.1	7:17:28.589	+37:46:23.88	3.100	1.69 ± 0.00	
16.2	7:17:26.050	+37:45:34.49	3.100	1.70 ± 0.22	
16.3	7:17:25.661	+37:45:13.43	3.100	0.85 ± 0.19	
17.1	7:17:28.646	+37:46:18.55	2.500	0.99 ± 0.05	
17.2	7:17:26.256	+37:45:31.82	2.500	2.93 ± 2.71	
17.3	7:17:25.966	+37:45:12.71	2.500	1.20 ± 0.27	
17.4	7:17:26.592	+37:45:29.84	2.500	2.98 ± 1.33	N
18.1	7:17:27.406	+37:46:07.10	2.400	1.69 ± 0.00	
18.2	7:17:26.683	+37:45:51.66	2.400	4.03 ± 0.26	
19.1	7:17:38.170	+37:45:16.87	6.387	4.62 ± 2.55	S,V
19.2	7:17:37.860	+37:44:33.87	6.387	3.55 ± 1.13	S,V
20.1	7:17:29.804	+37:45:54.42	5.000	1.04 ± 0.00	N
20.2	7:17:29.612	+37:45:52.62	5.000	2.09 ± 0.00	N
21.1	7:17:28.524	+37:45:17.94	2.000	5.59 ± 0.38	N
22.1	7:17:28.256	+37:45:21.23	1.500	2.83 ± 1.65	N
22.2	7:17:28.236	+37:45:19.91	1.500	4.47 ± 2.12	N
23.1	7:17:31.107	+37:45:46.47	3.000	1.20 ± 0.45	N
23.2	7:17:30.953	+37:45:43.14	3.000	3.68 ± 1.17	N
24.1	7:17:28.565	+37:45:08.76	3.000	0.66 ± 0.00	N
25.1	7:17:31.269	+37:44:41.10	4.500	2.33 ± 0.43	N
25.2	7:17:31.083	+37:44:33.92	4.500	4.03 ± 0.59	N
25.3	7:17:36.699	+37:45:59.07	4.500	0.46 ± 0.00	N
27.1	7:17:35.369	+37:44:52.50	2.000	2.06 ± 0.26	N
27.2	7:17:35.413	+37:44:51.16	2.000	0.66 ± 0.23	N
28.1	7:17:37.675	+37:43:58.70	2.000	1.67 ± 2.09	N
29.1	7:17:36.211	+37:44:35.43	1.800	2.80 ± 1.26	N
29.2	7:17:34.290	+37:44:18.97	1.800	2.73 ± 1.27	N
29.3	7:17:37.461	+37:44:59.83	1.800	2.57 ± 1.86	N
30.1	7:17:34.055	+37:44:20.78	1.800	2.77 ± 2.25	N
30.2	7:17:37.569	+37:45:03.96	1.800	2.32 ± 0.51	N
31.1	7:17:29.928	+37:45:22.68	1.750	2.17 ± 2.95	N
31.2	7:17:29.043	+37:45:01.98	1.750	3.56 ± 0.44	N
31.3	7:17:31.588	+37:45:53.94	1.750	2.25 ± 0.15	N
32.1	7:17:28.671	+37:45:27.87	2.700	4.00 ± 0.23	N
32.2	7:17:31.426	+37:46:09.57	2.700	0.75 ± 0.19	N
32.3	7:17:27.895	+37:44:56.93	2.700	2.53 ± 0.19	N
33.1	7:17:32.102	+37:45:29.53	5.000	4.38 ± 2.31	N
33.2	7:17:32.777	+37:45:50.83	5.000	0.94 ± 0.30	N
33.3	7:17:28.884	+37:44:19.29	5.000	1.20 ± 0.27	N
34.2	7:17:30.979	+37:45:04.33	2.300	5.44 ± 0.36	N
34.3	7:17:29.592	+37:44:39.16	2.300	0.44 ± 0.27	N
36.1	7:17:27.446	+37:46:19.25	2.500	2.09 ± 0.00	N
36.2	7:17:25.974	+37:45:47.89	2.500	3.74 ± 0.13	N
36.3	7:17:24.797	+37:45:21.06	2.500	2.01 ± 0.32	N
37.1	7:17:35.305	+37:45:17.08	4.000	1.77 ± 1.54	N
37.2	7:17:35.203	+37:45:17.08	4.000	2.94 ± 1.77	N
39.1	7:17:36.881	+37:43:54.51	2.000	0.97 ± 0.50	N
40.1	7:17:40.154	+37:43:36.19	3.000	0.46 ± 0.00	N
41.1	7:17:37.978	+37:43:41.06	3.000	0.46 ± 0.00	N
42.1	7:17:39.220	+37:44:01.71	3.000	0.46 ± 0.00	N
43.1	7:17:34.668	+37:43:44.25	3.000	3.70 ± 1.60	N
44.1	7:17:36.658	+37:43:58.23	2.000	3.00 ± 2.36	N
45.1	7:17:33.556	+37:44:21.12	3.000	7.96 ± 0.91	N

Table A1 – *continued*

ID	RAJ2000 (h:m:s)	Dec.2000 (d:m:s)	z	Error (arcsec)	Notes
45.2	7:17:32.029	+37:44:16.37	3.000	2.53 ± 0.33	N
45.3	7:17:37.071	+37:45:43.00	3.000	2.27 ± 0.50	N
47.1	7:17:38.397	+37:43:35.46	3.000	0.46 ± 0.00	N
49.1	7:17:36.709	+37:43:59.64	3.000	2.66 ± 0.83	N
49.2	7:17:34.316	+37:43:50.64	3.000	4.55 ± 0.93	N
50.1	7:17:29.866	+37:44:37.45	3.000	1.52 ± 0.20	N
50.2	7:17:31.100	+37:45:02.55	3.000	2.72 ± 0.44	N
50.3	7:17:34.273	+37:46:01.85	3.000	1.04 ± 0.00	N
52.1	7:17:28.407	+37:46:18.27	3.000	1.66 ± 0.26	N
52.2	7:17:26.455	+37:45:37.79	3.000	0.86 ± 0.11	N
52.3	7:17:25.689	+37:45:08.95	3.000	1.20 ± 0.27	N

Table A2. Like Table A1 but for the additional candidate systems not used in the main analysis of this work. At the time of submission of this paper, additional observations in the optical bands have been made available that has allowed us to uncover new additional candidate systems. All these systems are in excellent agreement with the model presented in this paper so their inclusion in the analysis should result in small changes to the mass model. Stamps of these systems are also provided in the website (http://www.ifca.unican.es/users/jdiego/MACS0717). These systems, together with the new ones that may be identified after the impending release of the new IR data, will be used in a subsequent paper.

ID	RAJ2000(h:m:s)	Dec.J2000(d:m:s)	z	Error (arcsec)
53.1	7:17:28.843	+37:45:40.60	2.7	5.35 ± 0.36
53.2	7:17:31.035	+37:46:05.71	2.7	0.35 ± 0.38
53.3	7:17:27.619	+37:44:49.79	2.7	2.73 ± 0.15
54.1	7:17:36.038	+37:44:42.81	1.2	3.40 ± 1.60
54.2	7:17:35.881	+37:44:40.50	1.2	3.19 ± 2.18
55.1	7:17:37.391	+37:43:54.66	5.0	3.26 ± 2.39
55.2	7:17:35.290	+37:43:44.35	5.0	2.89 ± 1.29
56.1	7:17:34.354	+37:45:46.06	5.0	8.87 ± 4.78
56.2	7:17:32.964	+37:45:21.47	5.0	10.82 ± 1.53
56.3	7:17:30.180	+37:44:08.24	5.0	1.96 ± 0.33
57.1	7:17:34.318	+37:45:43.93	5.0	10.44 ± 2.61
57.2	7:17:33.131	+37:45:23.45	5.0	12.75 ± 1.51
57.3	7:17:30.225	+37:44:06.47	5.0	2.52 ± 0.19
58.1	7:17:34.321	+37:45:44.60	5.0	7.29 ± 2.62
58.2	7:17:33.078	+37:45:23.01	5.0	12.83 ± 1.54
58.3	7:17:30.197	+37:44:06.64	5.0	2.36 ± 0.34
59.1	7:17:34.271	+37:45:45.49	4.0	4.13 ± 0.59
59.2	7:17:33.116	+37:45:24.60	4.0	3.88 ± 0.95
60.1	7:17:36.614	+37:45:48.98	2.6	0.61 ± 0.25
60.2	7:17:31.455	+37:44:26.40	2.6	2.48 ± 0.64
60.3	7:17:31.351	+37:44:28.87	2.6	1.75 ± 1.48
60.4	7:17:32.930	+37:44:28.56	2.6	0.84 ± 0.22
60.5	7:17:31.846	+37:44:40.95	2.6	4.38 ± 0.58
61.1	7:17:34.125	+37:45:37.75	2.4	2.65 ± 1.47
61.2	7:17:33.448	+37:45:26.19	2.4	4.36 ± 1.36
62.1	7:17:31.082	+37:44:42.36	3.0	0.66 ± 0.00
62.2	7:17:30.965	+37:44:38.74	3.0	3.77 ± 0.00
63.1	7:17:29.413	+37:44:58.33	3.0	5.97 ± 1.63
63.2	7:17:29.588	+37:45:04.63	3.0	0.96 ± 0.04
64.1	7:17:33.044	+37:44:19.95	2.5	6.11 ± 0.31
64.2	7:17:32.146	+37:44:18.22	2.5	5.39 ± 0.41
65.1	7:17:33.272	+37:44:21.32	4.0	1.68 ± 0.25
65.2	7:17:31.682	+37:44:18.37	4.0	6.74 ± 0.79

Table A3. Positions predicted by the lens model for several counter-images but with no clear counterpart in the optical image although possible candidates can be found in the neighbourhood of these positions. The associated uncertainty (in arcseconds) are shown in the last column. The errors represent the dispersion in the image plane of the predicted positions by the four models described in the paper while the tabulated values for RA and Dec. correspond to the average of the four predicted positions. The uncertainty can be compared with the typical error between observed and predicted arcs which is estimated to be ≈2.8 arcsec (see Section 6).

ID	RAJ2000(h:m:s)	Dec.J2000(d:m:s)	Error(arcsec)
2.3	7:17:32.661	37:44:15.401	0.45
2.4	7:17:37.413	37:45:35.088	2.84
18.3	7:17:25.389	37:45:9.424	0.44
19.3	7:17:31.693	37:44:0.284	0.55
20.3	7:17:26.831	37:44:38.956	0.44
21.2	7:17:31.109	37:46:6.378	0.31
22.3	7:17:29.035	37:45:38.956	0.20
22.4	7:17:29.865	37:45:53.721	0.61
23.3	7:17:28.066	37:44:35.088	0.57
24.2	7:17:32.196	37:46:13.057	0.41
25.4	7:17:32.878	37:44:27.823	0.39
27.3	7:17:32.285	37:44:14.229	1.34
27.4	7:17:36.109	37:44:40.479	0.81
27.5	7:17:37.058	37:45:23.018	2.40
30.3	7:17:36.099	37:44:36.378	2.98
34.1	7:17:33.090	37:45:55.360	1.10
37.3	7:17:31.248	37:44:4.385	1.15
37.4	7:17:37.591	37:45:13.174	7.37
59.3	7:17:30.181	37:44:13.057	0.41
61.3	7:17:30.556	37:44:18.917	0.41
62.3	7:17:35.961	37:45:55.362	0.79
63.3	7:17:33.165	37:46:9.073	0.23
64.3	7:17:37.107	37:45:40.831	0.44
65.3	7:17:37.354	37:45:48.565	1.14

Table A3 – *continued*

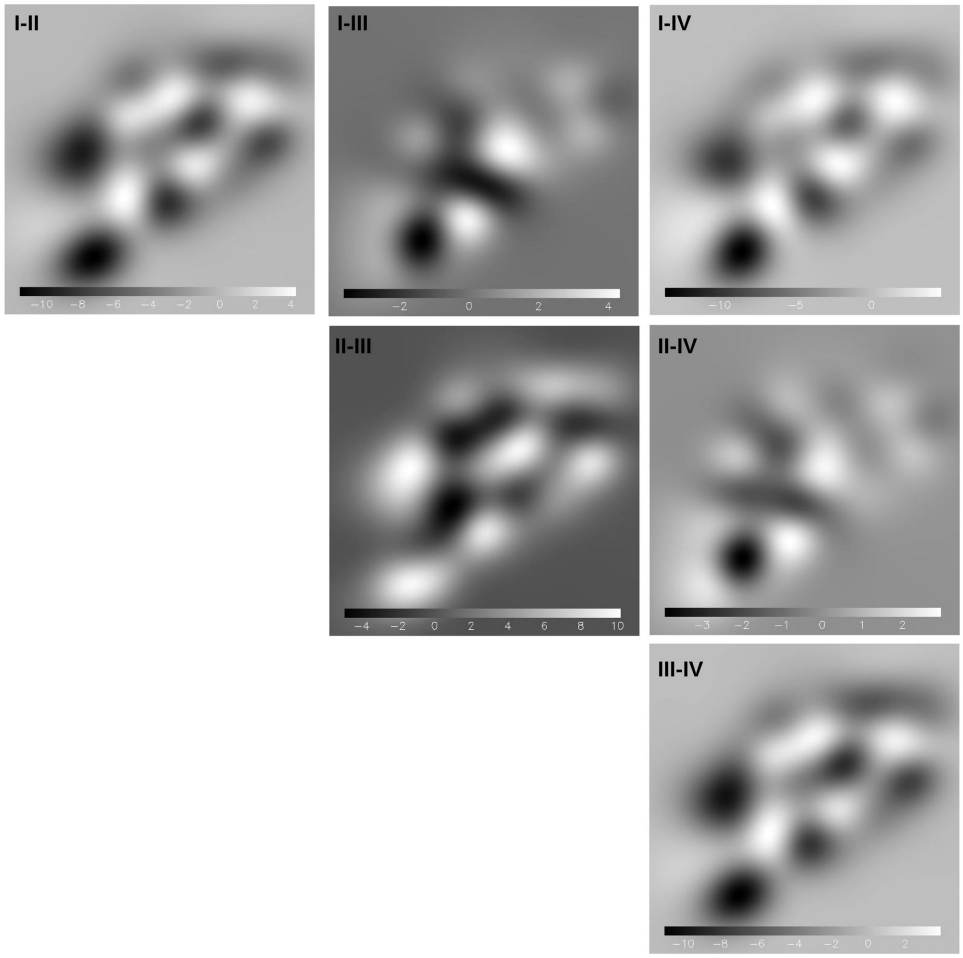

Figure A1. Normalized differences (in percent) between the models I, II, III, and IV.

This paper has been typeset from a TEX/LATEX file prepared by the author.